

## PAPER



Cite this: *J. Anal. At. Spectrom.*, 2023, **38**, 751

Received 23rd November 2022  
Accepted 23rd January 2023

DOI: 10.1039/d2ja00387b

rsc.li/jaas

# M-subshell X-ray production cross sections of Re and Os by electron impact

Alfredo Aguilar, Gustavo Castellano,  Silvina Segui, Jorge Trincavelli and Alejo Carreras \*

X-ray production cross sections were experimentally determined for the five M subshells of Re and Os by electron impact. Incident beam energies between 2.5 and 28 keV were used for this purpose, irradiating Re and Os thick targets in a scanning electron microscope. X-ray emission spectra were recorded with an energy dispersive spectrometer, and were processed through a careful parameter optimization routine previously developed. The X-ray production cross sections were then determined through an approach which involves an analytical function predicting the measured spectra through calculations based on the ionization depth distribution function. The results obtained were compared with empirical and theoretical predictions by means of relaxation data taken from the literature.

## 1 Introduction

Inner shell ionization–relaxation processes bear an inherent relevance in atomic physics, and their description permits validation of different theoretical approaches. In addition, several parameters related to these processes are involved in a number of algorithms required for atomic spectroscopy techniques, such as Auger spectroscopy or electron probe microanalysis. Among all these parameters, the ionization cross sections  $\sigma$  are of particular interest in the field of radiation transport in matter; these magnitudes may be assessed by theoretical calculations, although experiments can provide X-ray production cross sections  $\sigma^X$ , closely related to  $\sigma$ , as detailed below.

In the case of keV electrons, M-shell ionizations are those involved when irradiating heavy elements. Nevertheless, experimental data for  $\sigma^X$  have been scarcely reported, and it is necessary to rely on theoretical estimates for  $\sigma$ , for example, the distorted wave Born approximation (DWBA) which is valid in the energy range close to the ionization threshold, where the relativistic plane-wave Born approximation (PWBA) is expected to fail. In analytical techniques based on X-ray or Auger-electron emission, this is exactly the energy range of interest. Experimental determinations of M-shell X-ray production cross sections have been reported in the literature, mainly for very high incident electron energies,<sup>1,2</sup> as pointed out in ref. 3. Recently, some absolute measurements were performed at low overvoltages for Au, Bi,<sup>3</sup> Pb,<sup>4</sup> Th<sup>5</sup> and U,<sup>6</sup> by means of the thin target approach, in which a direct assessment of cross sections

is carried out when the target thickness can be determined accurately.

To overcome the experimental difficulties concerning the realization of thin samples, and the determination of the areal density, a bulk sample approach may be chosen. This strategy also helps in avoiding some uncertainties associated with the contribution of backscattering from the supporting substrate. For instance, An *et al.* used thick targets to determine K-shell ionization cross sections of Ni<sup>7</sup> by electron impact. The formalism used by An *et al.* is, however, particularly suitable for protons.<sup>8</sup>

In a recent study,  $\sigma^X$  values for M<sub>3</sub>, M<sub>4</sub> and M<sub>5</sub> subshells of Pt and Au by electron incidence were experimentally determined through a different method based on ionization depth distribution functions, also using thick targets.<sup>9</sup> In the present work, this new approach has been used to determine X-ray production cross sections for the five M subshells of Re and Os, which have been experimentally obtained for the first time. To this end, X-ray spectra induced by electron incidence at different energies were measured with an energy dispersive detector. These spectra were then processed by means of a robust optimization procedure previously developed,<sup>10</sup> taking special care in the continuum spectral description, as detailed below.

## 2 Experimental

X-ray emission spectra were obtained from pure Re and Os bulk standards (Micro-Analysis Consultants Ltd). According to the information provided by the manufacturers, the low level of impurities present in these standards permits us to neglect them for the purposes of the present work. Since these polished standards are embedded together in a non-conductive resin within a brass block, carbon coating was required to ensure

*Instituto de Física Enrique Gaviola (IFEG-CONICET), Facultad de Matemática, Astronomía, Física y Computación (FAMAF), Universidad Nacional de Córdoba, Córdoba, Argentina. E-mail: alejocarreras@unc.edu.ar*

adequate conductivity. These targets were irradiated with keV electron beams in a Carl Zeiss Sigma field emission scanning microscope. The X-ray spectra were acquired with an energy dispersive spectrometer (EDS), consisting of an Aztec characterization software controlling an Oxford silicon drift detector, whose front window is an ultrathin polymer layer, supported by a silicon grid 380  $\mu\text{m}$  thick with 77% open area.

The incident energies chosen were distributed between 2.5 and 28 keV, with acquisition live times ranging from 120 to 360 s and beam currents from 140 to 1100 pA, intended to achieve appropriate statistics in each case. As an example, Fig. 1 shows the Re spectrum induced using a 20 keV electron beam.

### 3 Methodology

By means of a spectral processing tool previously implemented in the software POEMA,<sup>10</sup> the X-ray production cross sections were determined from the experimental data. This procedure ensures the adequate description of the experimental spectrum through a reliable analytical function, in which several parameters may be optimized, among which are the sought magnitudes: the X-ray production cross sections are therefore obtained as a result of the optimization procedure. The spectral processing method was detailed in a recent contribution.<sup>9</sup> A brief description is given in this section, including some features specific to this work.

#### 3.1 Analytical description of spectra

The experimental spectrum  $I$  is estimated through an analytical expression  $\tilde{I}$ , which depends on the energy  $E_i$  associated with channel  $i$ :

$$\tilde{I}_i = B(E_i) + \sum_q P_q S_q(E_i), \quad (1)$$

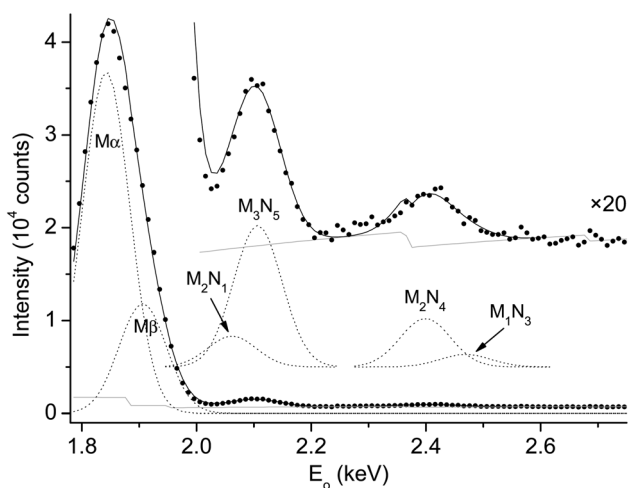


Fig. 1 Rhenium M X-ray spectrum for a 20 keV electron beam. Magnified images of the weak peaks are also shown. Dots: experimental data; solid black line: fit; dotted lines: individual contribution of each transition; solid grey line: background.

where  $B$  is the background contribution,  $P_q$  is the characteristic  $q$  line intensity, and  $S_q$  is a Gaussian function representing the instrumental broadening.

Actually, it is well known that characteristic peaks show an asymmetric behavior at the low energy side due to incomplete charge collection in the detector,<sup>11</sup> particularly noticeable for the most intense peaks. Nevertheless, for the  $M\alpha$  line, this small asymmetry overlaps with the  $M_3N_1$  line, which hampers the correct determination of  $M_3$ -group line intensities. To overcome this inconvenience, the asymmetric region was excluded from the analyzed spectra. The fitted region is shown in Fig. 1.

**3.1.1 Bremsstrahlung emission.** The bremsstrahlung contribution was described by using an empirical model previously developed,<sup>12</sup> which works properly in a wide range of atomic numbers, and electron and photon energies. Nevertheless, in this study it was necessary to add a polynomial correction, particularly for a better description of weak lines, *i.e.*, with a low peak-to-background ratio.

**3.1.2 Characteristic emission.** The intensity corresponding to the characteristic  $q$  decay to the  $M_\ell$  shell can be expressed as

$$p_q = C_\ell P_q(ZAF)_q \varepsilon(E_q), \quad (2)$$

where  $p_q$  and  $E_q$  are, respectively, the relative transition probability and the characteristic energy for this emission;  $Z$ ,  $A$  and  $F$  are associated with the atomic number, and absorption and fluorescence correction factors;<sup>13</sup> and  $\varepsilon$  is the spectrometer's intrinsic efficiency, which can be considered constant in the energy range of interest. It is important to stress that all details concerning backscattering losses, multiple scattering effects, *etc.*, are included in the peak intensity assessment through the ionization depth-distribution function, as detailed in ref. 10. The peak scale factor  $C_\ell$  involves the number of incident electrons  $N_e$  and the X-ray production cross section corresponding to the  $M_\ell$  shell  $\sigma_\ell^X$

$$C_\ell = N_e \sigma_\ell^X \frac{\Delta\Omega}{4\pi}, \quad (3)$$

$\Delta\Omega$  is the solid angle subtended by the detector.

**3.1.3 Carbon coating.** As mentioned above (see §2), the standard set is coated with carbon to allow for good conductivity. This carbon coating degrades the incident electron beam and modifies the emerging X-ray intensity. To account for the influence of this effect, the conductive layer thickness must be properly known. To this aim, the electron beam was directed to a region of the brass mount close to the analyzed standards. The resulting spectrum was processed using the software POEMA to obtain the carbon coating thickness, which resulted in  $z_c = (22.1 \pm 0.8)$  nm, the uncertainty being assessed using the software as detailed in ref. 14.

The effective energy of the electrons traversing the carbon layer to reach the Re or Os standard surface, was estimated by determining the Duane–Hunt limit  $E_{DH}$ <sup>15</sup> and the energy loss in the carbon layer. Each  $E_{DH}$  value was determined through a linear fit to find the spectral intercept with zero intensity. On the other hand, the energy loss in the carbon layer was estimated as the product of the stopping power  $S$  of carbon at  $E_{DH}$

by the mass thickness of the layer  $\rho z_c$ . Thus, the energy  $E_o$  of the electrons reaching the standard surface can be written as

$$E_o = E_{\text{DH}} - S\rho z_c \quad (4)$$

### 3.2 Parameter refinement procedure

The spectral processing consisted in fitting the analytical function (1) to the experimental data, by optimizing the parameters involved in (1) and (2). The X-ray production cross sections  $\sigma_\ell^x$  were obtained from the parameters  $C_\ell$  included in eqn (3).

For each of the studied elements, the relative transition probabilities  $p_q$  corresponding to diagram lines were refined for the 20 keV spectrum, except for the lines corresponding to the  $M_3$  group, which were taken from Perkins *et al.*,<sup>16</sup> since the  $M_3N_1$  line is strongly overlapped with the asymmetric  $M\alpha$  tail. These  $p_q$  values were kept fixed for all the other incidence energies. For Re, the  $p_q$  values obtained were 0.98 for  $M\alpha$  ( $M_5N_{6,7}$ ), 0.91 for  $M\beta$  ( $M_4N_6$ ), 0.80 for  $M_3N_5$ , 0.57 for  $M_2N_4$  and 1 for  $M_1N_3$  (only one emission recorded); whereas for Os the resulting values for  $p_q$  were 0.97 for  $M\alpha$  ( $M_5N_{6,7}$ ), 0.89 for  $M\beta$  ( $M_4N_6$ ), 0.72 for  $M_3N_5$ , 0.84 for  $M_2N_4$  and 1 for  $M_1N_3$  (also one line). Bearing these values in mind, in order to obtain the  $q$ -line production cross section (for  $q = M\alpha, M\beta, M_3N_5, M_2N_4, M_1N_3$ ), each  $\sigma_\ell^x$  must be multiplied by the transition rate  $p_q$  corresponding to this decay. It must be stressed that these transition rates are only valid for the present purpose, since with an energy resolution better than that of the EDS used, more decays may be identified using the spectrometer.

Finally, most characteristic energies  $E_q$  were taken from Bearden's work.<sup>17</sup> Instead, for the  $M_4N_3$  Os line and  $M_1N_3, M_2N_1, M_2N_4$  and  $M_3N_1$  Re lines, the energies compiled by Perkins *et al.*<sup>16</sup> were used, because these values are absent in Bearden tabulation. In addition, the  $M_2N_4$  Os characteristic energy was also taken from Perkins *et al.*,<sup>16</sup> in view of its better agreement with the peak position in the measured spectra. All the characteristic energies were kept fixed during the optimization procedure.

The optimization routine consisted, in the first step, in refining the peak scale factors  $C_\ell$  corresponding to the  $M_3, M_4$  and  $M_5$  subshells in the wide spectral region shown in Fig. 1, while in the second step, the  $C_\ell$  factors corresponding to  $M_1$  and  $M_2$  were optimized in a smaller region, since these peak scale factors are particularly sensitive to the intensity of the continuum in the case of weak lines. This care permitted an adequate description of these less likely emissions, and thus enabled the determination of the cross sections for these subshells, which was not possible in previous work.<sup>9</sup>

## 4 Results and discussion

The values obtained for the X-ray production cross sections corresponding to all five M subshells of Re and Os are shown in Tables 1 and 2, and in Fig. 2 and 3, respectively.

The uncertainty associated with the X-ray production cross section was estimated according to eqn (3), by propagation of

**Table 1** X-ray production cross sections of rhenium. Numbers in parentheses indicate the estimated uncertainties in the last digits. The uncertainties associated with incident energies are below 0.5%

$E_o$ (keV)	$\sigma_1^x$ (barns)	$\sigma_2^x$ (barns)	$\sigma_3^x$ (barns)	$\sigma_4^x$ (barns)	$\sigma_5^x$ (barns)
2.231	—	—	—	122(9)	370(30)
2.772	—	—	15(4)	230(40)	590(90)
3.286	—	9.5(4)	20(3)	300(30)	740(60)
3.822	—	14.6(6)	31(4)	340(20)	810(50)
4.85	1.5(2)	18(1)	39(3)	390(20)	880(50)
5.889	0.9(2)	22(2)	39(3)	410(30)	870(40)
6.897	1.5(2)	21(2)	39(3)	420(30)	850(40)
7.9	2.0(3)	20(2)	39(3)	420(30)	810(40)
8.924	2.0(3)	20(2)	39(3)	420(30)	770(40)
9.957	2.0(4)	21(2)	38(3)	410(30)	750(40)
11.978	2.1(4)	15(2)	35(3)	360(20)	590(30)
14.917	1.9(6)	12(2)	29(3)	310(30)	470(30)
20.008	1.9(9)	13(3)	28(3)	320(30)	440(20)
27.73	1.4(1.1)	11(2)	25(5)	300(30)	340(40)

the errors corresponding to the number of incident electrons  $N_e$ , the detector solid angle  $\Delta\Omega$ , and the peak scale factor  $C_\ell$  obtained from the spectral fitting. The uncertainty of the latter, in turn, was obtained by propagating the errors in the experimental intensities  $I_i$ , through numerical differentiation.<sup>14</sup>

On the other hand, the error in  $E_o$ , always below 0.5%, was estimated by propagating the uncertainties of  $E_{\text{DH}}$  and  $z_c$  in eqn (4). In turn, the uncertainty associated with  $E_{\text{DH}}$  was assessed from error propagation in the parameters involved in the linear fit performed to obtain the Duane–Hunt energy.

To the best of the authors' knowledge, no experimental data are available in the literature for the individual M-subshell X-ray production cross sections of the elements studied here. To compare with theoretical or empirical data derived from the ionization cross sections  $\sigma_\ell$ , it is necessary to rely on several relaxation parameters known with poor precision, namely, the fluorescence yields  $\omega_\ell$  and the Coster–Kronig transition probabilities  $f_{ij}^x$  from  $M_j$  to  $M_i$  subshells. The X-ray production cross section  $\sigma_\ell^x$  is related to the final vacancy production cross

**Table 2** X-ray production cross sections of osmium. Numbers in parentheses indicate the estimated uncertainties in the last digits. The uncertainties associated with incident energies are below 0.5%

$E_o$ (keV)	$\sigma_1^x$ (barns)	$\sigma_2^x$ (barns)	$\sigma_3^x$ (barns)	$\sigma_4^x$ (barns)	$\sigma_5^x$ (barns)
2.23	—	—	—	140(10)	290(20)
2.78	—	—	4(2)	260(50)	500(90)
3.304	—	3.0(1)	24(2)	370(20)	660(40)
3.832	—	8.6(4)	34(2)	440(20)	750(40)
4.85	1.2(2)	12(2)	46(3)	530(30)	840(40)
5.89	1.7(3)	14(2)	43(2)	550(30)	850(40)
6.884	2.8(5)	13(2)	44(2)	560(30)	830(40)
7.905	2.6(4)	13(2)	47(3)	560(30)	800(40)
8.934	1.8(2)	14(2)	49(3)	560(30)	760(40)
9.932	2.5(3)	14(2)	47(2)	570(30)	750(30)
11.929	1.0(2)	12(3)	43(3)	410(20)	640(30)
14.896	0.7(2)	10(3)	33(3)	360(30)	500(30)
19.938	0.9(4)	9(4)	32(3)	380(30)	450(20)
28.022	1(1)	7(3)	30(10)	380(40)	360(40)

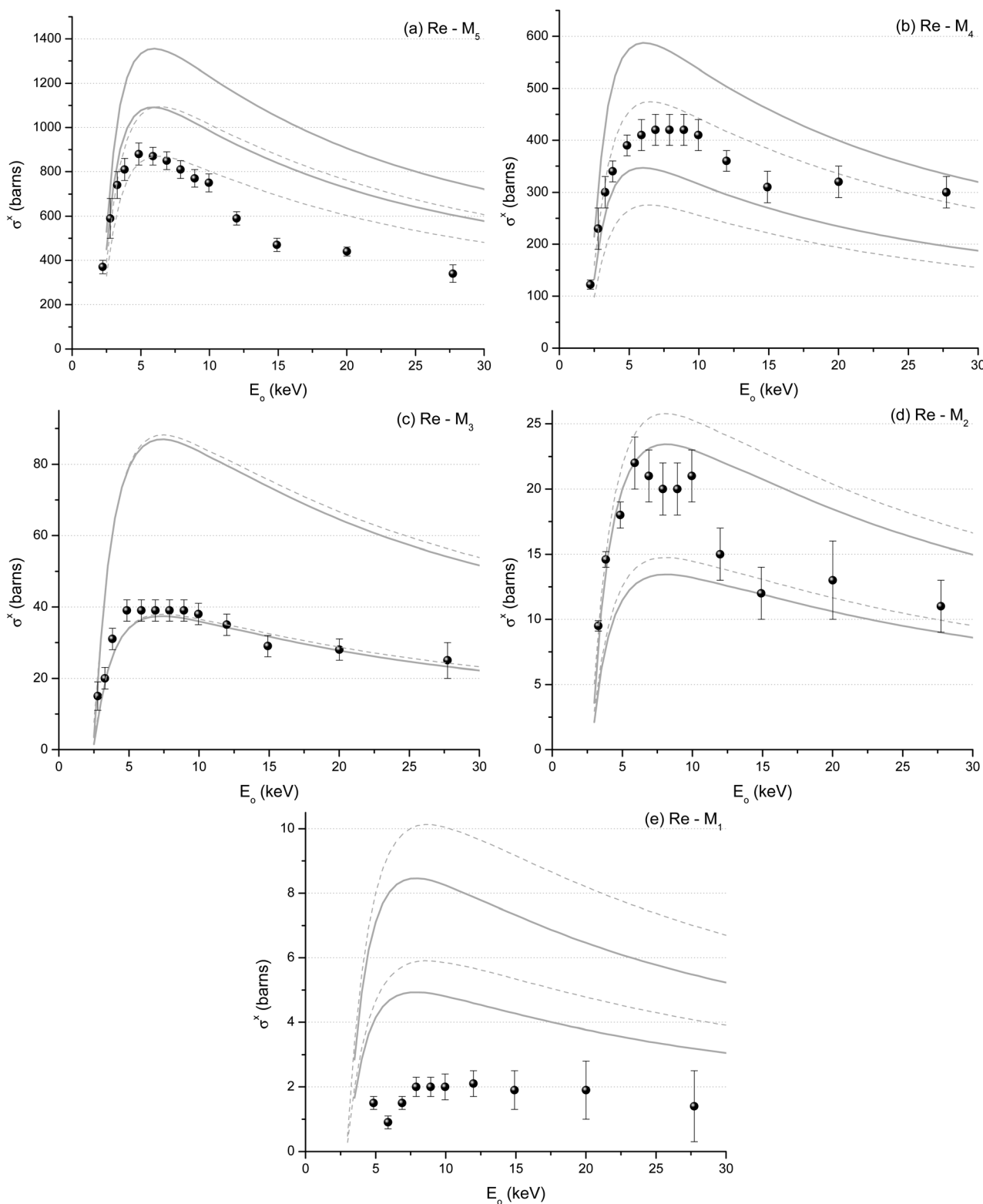


Fig. 2 Rhenium X-ray production cross section. Solid spheres: present data. The gray lines delimitate regions where results for  $\sigma^x$  derived from theoretical or empirical data for ionization cross sections  $\sigma$  can be obtained when different combinations of relaxation parameters are used; solid line: Bote and Salvat,<sup>18</sup> dashed line: Casnati *et al.*<sup>19</sup> (a)  $M_5$  subshell; (b)  $M_4$  subshell; (c)  $M_3$  subshell; (d)  $M_2$  subshell; (e)  $M_1$  subshell.

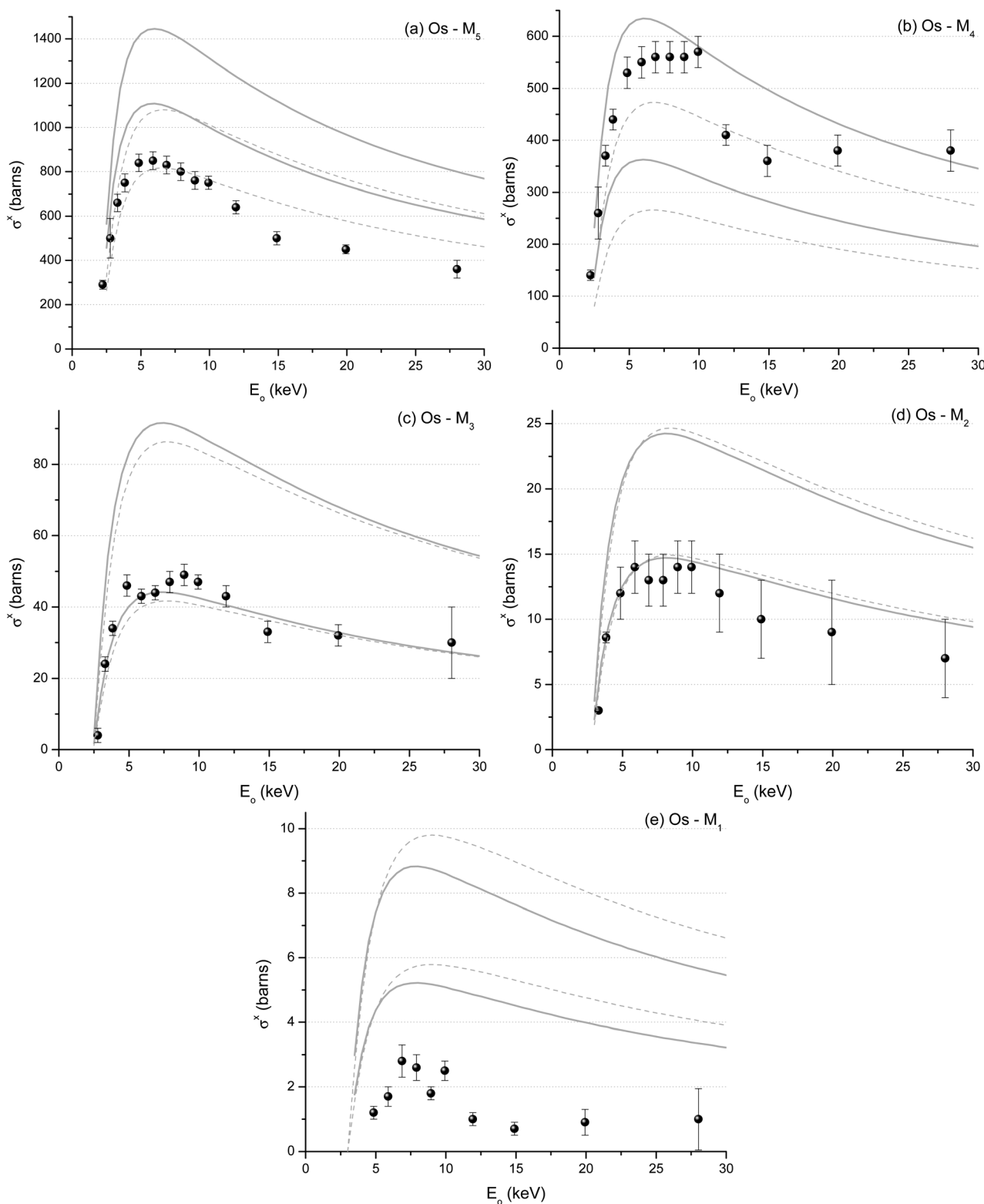


Fig. 3 Osmium X-ray production cross section. Solid spheres: present data. The gray lines delimitate regions where results for  $\sigma^x$  derived from theoretical or empirical data for ionization cross sections  $\sigma$  can be obtained when different combinations of relaxation parameters are used; solid line: Bote and Salvat,<sup>18</sup> dashed line: Casnati *et al.*<sup>19</sup> (a)  $M_5$  subshell; (b)  $M_4$  subshell; (c)  $M_3$  subshell; (d)  $M_2$  subshell; (e)  $M_1$  subshell.

Table 3 Coster–Kronig coefficients and fluorescence yields used for comparison

Elem	Ref.	$\omega_{M_1}$	$\omega_{M_2}$	$\omega_{M_3}$	$\omega_{M_4}$	$\omega_{M_5}$	$f_{45}$	$S_{12}$	$S_{13}$	$S_{14}$	$S_{15}$	$S_{23}$	$S_{24}$	$S_{25}$	$S_{34}$	$S_{35}$
Re	16	0.00269	0.00505	0.00630	0.0216	0.0228	0.109	0.128	0.590	0.077	0.108	0.088	0.575	0.094	0.068	0.620
Re	24	0.00157	0.00298	0.00271												
Re	20				0.0134	0.0228	0.449	0.168	0.553	0.073	0.121	0.114	0.702	0.075	0.119	0.778
Os	16	0.00281	0.00526	0.00662	0.0234	0.0245	0.102	0.128	0.591	0.077	0.108	0.088	0.574	0.093	0.068	0.617
Os	24	0.00166	0.00326	0.00320												
Os	20				0.0140	0.0233	0.435	0.158	0.559	0.072	0.121	0.115	0.701	0.072	0.114	0.780

section  $\tilde{\sigma}_\ell$  using  $\sigma_\ell^X = \omega_\ell \tilde{\sigma}_\ell$ , the latter being connected to  $\sigma_\ell$  as follows:

$$\begin{aligned}\tilde{\sigma}_1 &= \sigma_1 \\ \tilde{\sigma}_2 &= \sigma_2 + f_{12}\tilde{\sigma}_1 \\ \tilde{\sigma}_3 &= \sigma_3 + f_{13}\tilde{\sigma}_1 + f_{23}\tilde{\sigma}_2 \\ \tilde{\sigma}_4 &= \sigma_4 + f_{14}\tilde{\sigma}_1 + f_{24}\tilde{\sigma}_2 + f_{34}\tilde{\sigma}_3 \\ \tilde{\sigma}_5 &= \sigma_5 + f_{15}\tilde{\sigma}_1 + f_{25}\tilde{\sigma}_2 + f_{35}\tilde{\sigma}_3 + f_{45}\tilde{\sigma}_4\end{aligned}$$

When the electron energies exceed the  $L_i$  ionization energy, vacancies can occur in this subshell, and decays from  $M_\ell$  to  $L_i$  must be taken into account. This implies that additional terms must complement each of the preceding formulae in these cases, which may be expressed in terms of the transition probabilities from  $M_\ell$  to  $L_i$  subshells,  $n_{L_i M_\ell}$

$$\sigma_{L_1 n_{L_1 M_\ell}} + \sigma_{L_2 n_{L_2 M_\ell}} + \sigma_{L_3 n_{L_3 M_\ell}}.$$

Obviously, K vacancies cannot be created for the beam energy range involved here.

The data published in the literature for fluorescence yields and Coster–Kronig probabilities bear certain discrepancies among them, maybe because of the difficulties of measuring them independently. For the present comparisons, values for  $\omega_\ell$ <sup>16,20</sup> and  $f_{ij}$ <sup>16,20–25</sup> provided in different sources were considered. Each model chosen for  $\sigma_\ell$  may be combined with different estimates for  $\omega_\ell$  and  $f_{ij}$  to produce a  $\sigma_\ell^X$  curve. The upper and lower bounds for these possible choices are displayed in Fig. 2 and 3, which involve the theoretical approach by Bote and Salvat<sup>18</sup> based on the DWBA formalism, and the empirical function given by Casnati *et al.*<sup>19</sup> The lower bound results when the  $f_{ij}$  probabilities given by Perkins *et al.*<sup>16</sup> are combined with the  $\omega_\ell$  values fitted by Kaur and Mittal<sup>24</sup> to McGuire's data;<sup>25</sup> the upper bound reflects the values obtained for  $\omega_\ell$  published by Perkins *et al.*<sup>16</sup> along with the  $f_{ij}$  data reported by Söğüt *et al.*<sup>20</sup> The set of all the relaxation parameters taken into account is displayed in Table 3. It is worth mentioning that some of the  $f_{ij}$  values taken for these assessments have in fact been extrapolated, outside the range within which they were recommended, as clearly shown in the cutoff/onset table included in ref. 21.

Fig. 2 and 3 evidence a clear discrepancy between the values resulting from the two sets of parameters chosen for the comparisons, particularly for the  $M_5$  subshell, and to a lower extent for  $M_4$  and  $M_1$ , whereas for the  $M_3$  and  $M_2$  subshells the predictions are indistinguishable. In addition, important differences occur when selecting different sets of relaxation parameters for the five subshells. It is thus clear that the alternative chosen for the relaxation parameters is key in the

determination of  $\sigma_\ell^X$  from the ionization cross sections  $\sigma_\ell$ , since rather wide variations occur within the ranges displayed in the graphs. Bearing these possible variations in mind, the values obtained in the present work are in reasonable agreement with the predictions available, except for the  $M_1$  subshell, for which the predictions are above the experimental results obtained here. It must be noted that the  $M_1 N_3$  line used to obtain the  $M_1$  X-ray production cross section is very weak, which suggests that the uncertainties shown in Fig. 2(e) and 3(e) could be underestimated.

It is worth noting that all Re and Os spectra are governed by an additional difficulty related to X-ray self-absorption, since the  $M_5$  level can be ionized by the  $M\beta$  emission, with a high efficiency. This suggests that the results obtained for high energies, where self-absorption is more important, might exhibit some kind of systematic error through the absorption correction factors implemented. This could explain the possible bias in the  $M_5$  and  $M_4$  curves, which in the case of a 28 keV electron beam exhibit an apparent crossover in the osmium cross sections obtained.

All the inconveniences mentioned, related to experimental limitations and to the spread of atomic and relaxation parameters found in the literature, must always be confronted with the simplifications assumed in the theoretical assessment of the ionization cross sections, which involve numerical approximations and assumptions regarding symmetry or asymptotic behaviors for the atomic potential, one-active-electron approximation, *etc.*

## 5 Conclusion

Experimental data for the X-ray production cross sections under electron irradiation have been obtained for individual Re- and Os-M subshells, which are unavailable in the literature, to the best of the authors' knowledge. To this aim, X-ray emission spectra were measured for keV electron beams impinging on bulk pure standards, and processed according to a method developed previously, which is based on the ionization depth distribution function.

An important inconvenience arises when contrasting the X-ray production cross sections obtained, with theoretical or empirical models for the ionization cross sections, since the rather large spread found in the literature for Coster–Kronig transition probabilities and fluorescence yields impedes a clear comparison between the experimental values and the ones produced from theoretical or empirical models. Since the

independent experimental determination of these relaxation parameters is almost impossible, a reliable data set of X-ray production cross sections for individual M subshells will only be achieved by means of a number of measurements for heavy elements through different approaches.

## Conflicts of interest

There are no conflicts to declare.

## Acknowledgments

This work was financially supported by the Secretaría de Ciencia y Técnica of the Universidad Nacional de Córdoba (UNC), Argentina, and also through a PICT2016 grant no. 0285, from ANPCyT-FONCyT, Argentina. The authors are also grateful to the Laboratorio de Microscopía y Análisis por Rayos X (LAMARX-UNC), where the experimental determinations were performed.

## References

- 1 K. Ishii, M. Kamiya, K. Sera, S. Morita, H. Tawara, M. Oyamada and T. C. Chu, *Phys. Rev. A*, 1977, **15**, 906–913.
- 2 D. H. H. Hoffmann, C. Brendel, H. Genz, W. Löw, S. Müller and A. Richter, *Z. Med. Phys.*, 1979, **293**, 187–201.
- 3 C. Merlet, X. Llovet and F. Salvat, *Phys. Rev. A: At., Mol., Opt. Phys.*, 2008, **78**, 022704.
- 4 A. Moy, C. Merlet, X. Llovet and O. Dugne, *J. Phys. B: At., Mol. Opt. Phys.*, 2013, **46**, 115202.
- 5 A. Moy, C. Merlet and O. Dugne, *Chem. Phys.*, 2014, **440**, 18–24.
- 6 A. Moy, C. Merlet, X. Llovet and O. Dugne, *J. Phys. B: At., Mol. Opt. Phys.*, 2014, **47**, 055202.
- 7 Z. An, Y. Wu, M. Liu, Y. Duan and C. Tang, *Nucl. Instrum. Methods Phys. Res. Sect. B Beam Interact. Mater. Atoms*, 2006, **246**, 281–287.
- 8 P. D. Pérez, T. P. Rodríguez, J. Trincavelli, J. M. Fernández-Varea and S. G. Suárez, *J. Anal. At. Spectrom.*, 2019, **34**, 214–221.
- 9 A. Carreras, G. Castellano, S. Segui and J. Trincavelli, *Phys. Rev. A*, 2020, **102**, 012817.
- 10 R. Bonetto, G. Castellano and J. Trincavelli, *X-Ray Spectrom.*, 2001, **30**, 313–319.
- 11 C. Visňovezky, S. Limandri, M. E. Canafoglia, R. Bonetto and J. Trincavelli, *Spectrochim. Acta, Part B*, 2007, **62**, 492–498.
- 12 G. Castellano, J. Osán and J. Trincavelli, *Spectrochim. Acta, Part B*, 2004, **59**, 313–319.
- 13 V. Scott, G. Love and S. Reed, *Quantitative Electron-Probe Microanalysis*, Ellis Horwood, London, 2nd edn, 1995.
- 14 R. D. Bonetto, A. C. Carreras, J. C. Trincavelli and G. E. Castellano, *J. Phys. B*, 2004, **37**, 1477.
- 15 W. Duane and F. Hunt, *Phys. Rev.*, 1915, **6**, 166–172.
- 16 S. T. Perkins, D. E. Cullen, M. H. Chen, J. H. Hubbell, J. Rathkopf and J. H. Scofield, Tables and graphs of atomic subshell and relaxation data derived from the LLNL evaluated atomic data library (EADL), Z=1–100, *Lawrence Livermore National Laboratory Report*, 1991, UCRL-50400 30, 1.
- 17 J. A. Bearden, *Rev. Mod. Phys.*, 1967, **39**, 78.
- 18 D. Bote, F. Salvat, A. Jablonski and C. Powell, *At. Data Nucl. Data Tables*, 2009, **95**, 871–909.
- 19 E. Casnati, A. Tartari and C. Baraldi, *J. Phys. B: At. Mol. Phys.*, 1982, **15**, 155–167.
- 20 O. Söğüt, E. Büyükkasap, A. Küçükönder, M. Ertuğrul, O. Doğan, H. Erdoğan and O. Şimşek, *X-Ray Spectrom.*, 2002, **31**, 62–70.
- 21 Y. Chauhan and S. Puri, *At. Data Nucl. Data Tables*, 2008, **94**, 38–49.
- 22 M. H. Chen, B. Crasemann and H. Mark, *Phys. Rev. A*, 1980, **21**, 449–453.
- 23 M. H. Chen, B. Crasemann and H. Mark, *Phys. Rev. A*, 1983, **27**, 2989–2994.
- 24 G. Kaur and R. Mittal, *J. Quant. Spectrosc. Radiat. Transfer*, 2014, **133**, 489–503.
- 25 E. McGuire, *Phys. Rev. A*, 1972, **5**, 1043–1047.